^{89}Zr-3,2-HOPO-Mesothelin Antibody PET Imaging Reflects Tumor Uptake of Mesothelin-Targeted ^{227}Th-Conjugate Therapy in Mice

Linda N. Broer[1], Daan G. Knapen[1], Frans V. Suurs[1], Ingrid Moen[2], Danique Giesen[1], Stijn J.H. Waaijer[1], Baard Indrevoll[2], Christine Ellingsen[2], Alexander Kristian[2], Alan S. Cuthbertson[2], Derk-Jan A. de Groot[1], Patricia E. Cole[3], Elisabeth G.E. de Vries[1], Urs B. Hagemann[4], and Marjolijn N. Lub-de Hooge[5,6]

[1]*Department of Medical Oncology, University Medical Center Groningen, University of Groningen, Groningen, The Netherlands;* [2]*Bayer AS, Oslo, Norway;* [3]*Bayer U.S., LLC, Whippany, New Jersey;* [4]*Bayer AG, Berlin, Germany;* [5]*Department of Clinical Pharmacy and Pharmacology, University Medical Center Groningen, University of Groningen, Groningen, The Netherlands; and* [6]*Department of Nuclear Medicine and Molecular Imaging, University Medical Center Groningen, University of Groningen, Groningen, The Netherlands*

The mesothelin (MSLN)-targeted ^{227}Th conjugate is a novel α-therapy developed to treat MSLN-overexpressing cancers. We radiolabeled the same antibody–chelator conjugate with ^{89}Zr to evaluate whether PET imaging with ^{89}Zr-MSLN matches ^{227}Th-MSLN tumor uptake, biodistribution, and antitumor activity. **Methods:** Serial PET imaging with protein doses of 4, 20, or 40 μg of ^{89}Zr-MSLN and ^{89}Zr-control was performed up to 168 h after tracer injection in human tumor–bearing nude mice with high (HT29-MSLN) and low (BxPc3) MSLN expression. ^{89}Zr-MSLN and ^{227}Th-MSLN ex vivo tumor uptake and biodistribution were compared at 6 time points in HT29-MSLN and in medium–MSLN-expressing (OVCAR-3) tumor–bearing mice. ^{89}Zr-MSLN PET imaging was performed before ^{227}Th-MSLN treatment in HT29-MSLN and BxPc3 tumor–bearing mice. **Results:** ^{89}Zr-MSLN PET imaging showed an SUV_{mean} of 2.2 ± 0.5 in HT29-MSLN tumors. Ex vivo tumor uptake was 10.6% ± 2.4% injected dose per gram at 168 h. ^{89}Zr-MSLN tumor uptake was higher than uptake of ^{89}Zr-control ($P = 0.0043$). ^{89}Zr-MSLN and ^{227}Th-MSLN showed comparable tumor uptake and biodistribution in OVCAR-3 and HT29-MSLN tumor–bearing mice. Pretreatment SUV_{mean} was 2.2 ± 0.2 in HT29-MSLN tumors, which decreased in volume on ^{227}Th-MSLN treatment. BxPc3 tumors showed an SUV_{mean} of 1.2 ± 0.3 and remained similar in size after ^{227}Th-MSLN treatment. **Conclusion:** ^{89}Zr-MSLN PET imaging reflected MSLN expression and matched ^{227}Th-MSLN tumor uptake and biodistribution. Our data support the clinical exploration of ^{89}Zr-MSLN PET imaging together with ^{227}Th-MSLN therapy, both using the same antibody–chelator conjugate.

Key Words: PET imaging; ^{89}Zr; targeted ^{227}Th therapy; antibody conjugate; mesothelin

J Nucl Med 2022; 63:1715–1721
DOI: 10.2967/jnumed.121.263079

Despite anticancer therapy advancements, several unmet medical needs remain. For instance, patients with mesothelioma and high-grade serous ovarian cancer would benefit from novel treatment options (*1,2*).

Recently, targeted α-therapy has emerged as a potential cancer treatment option. α-particle–emitting radionuclides targeted to the tumor enable potent antitumor activity while limiting toxicity to healthy tissues because of their high linear energy transfer and short range in tissue (*3,4*). Currently, ^{223}Ra-dichloride for metastatic castration-resistant prostate cancer is the only approved targeted α-therapy (*5,6*). Unlike ^{223}Ra, its progenitor ^{227}Th forms a stable complex with an *N*-methyl-3-hydroxypyridine-2-one (3,2-HOPO) chelator conjugated to tumor-associated antigen–targeting antibodies (*7–9*). Targeted ^{227}Th conjugates showed efficacy in mice, including those targeting mesothelin (MSLN), prostate-specific membrane antigen, CD33, and CD70 (*10–14*). Tumor-associated antigen binding of targeted ^{227}Th conjugates enables local tumor cell killing via double-strand DNA breaks caused by ^{227}Th decay (*9*).

MSLN is a glycosyl-phosphatidylinositol cell membrane–anchored protein involved in cell–cell adhesion and metastatic spread (*15–17*). MSLN expression by healthy tissues is limited to the peritoneum, pleura, and pericardium. However, it is overexpressed by several human cancers, such as mesothelioma and ovarian cancer (*18*). Therefore, MSLN is attractive for targeted cancer therapy, such as antibody–drug conjugates, chimeric antigen receptor T-cells, and targeted radionuclide therapy, currently tested in preclinical and clinical studies (*19–22*).

The MSLN-targeted ^{227}Th conjugate comprises 3,2-HOPO covalently attached to fully human anti-MSLN monoclonal antibody anetumab and stably complexed with the α-particle emitter ^{227}Th (*13*). The conjugate is reactive only to human MSLN. Understanding ^{227}Th-MSLN tumor uptake and biodistribution may be valuable to guide clinical development. PET can noninvasively visualize the biodistribution of monoclonal antibodies, also targeting MSLN (*23–25*). We developed a PET tracer complexing the 3,2-HOPO–MSLN conjugate with ^{89}Zr. By using the same antibody–chelator conjugate, we aim to avoid chelator-driven differences in pharmacokinetic properties. In mice bearing human MSLN–overexpressing tumors, we evaluated whether ^{89}Zr-MSLN PET was able to specifically visualize MSLN, whether this imaging could predict ^{227}Th-MSLN tumor uptake and biodistribution, and whether ^{89}Zr-MSLN tumor uptake matches ^{227}Th-MSLN antitumor activity.

Received Aug. 19, 2021; revision accepted Mar. 23, 2022.
For correspondence or reprints, contact Marjolijn N. Lub-de Hooge (m.n.de.hooge@umcg.nl).
Published online Apr. 14, 2022.

MATERIALS AND METHODS

Radiolabeling and Quality Control of ^{227}Th-MSLN, ^{89}Zr-MSLN, and ^{89}Zr-Control

The radionuclides ^{227}Th and ^{89}Zr were coupled to fully human IgG1 anti-MSLN monoclonal antibody and an IgG1-isotype control with 3,2-HOPO. This chelator is an octadentate with 4 bidentate 3,2-HOPO metal-complexation units and a carboxylic arm for monoclonal antibody conjugation, via amide coupling (*8*). Bayer AG provided conjugates 3,2-HOPO–MSLN and 3,2-HOPO–control with chelator-to-antibody ratios of 0.5. ^{227}Th radiolabeling of 3,2-HOPO–MSLN, resulting in ^{227}Th-MSLN, and quality control were performed as described previously (*13*). For PET studies, 3,2-HOPO–MSLN and 3,2-HOPO–control were radiolabeled with ^{89}Zr-oxalate (PerkinElmer) in 0.5 M 2-[4-(2-hydroxyethyl)piperazin-1-yl]ethanesulfonic acid, pH 6.7, for 1–2 h at 37°C. ^{89}Zr-MSLN tended to form radioactive dimers. For the 4-μg dose, the radioactive dimer formation was 10% at a 0.1 mg/mL antibody concentration, with protein desalting purification in 10 mM histidine and 130 mM glycine at pH 7.4 in water. The 20- and 40-μg dose preparation required higher antibody concentrations of 0.2 and 0.4 mg/mL during radiolabeling, resulting in 30% and 60% radioactive dimers, respectively. The effect of 60% and 10% radioactive dimer content on ^{89}Zr-MSLN biodistribution was compared at the 4-μg dose. To induce 60% dimers at this dose, an additional radiolabeling was performed at a 0.4 mg/mL concentration of antibody with purification via Vivaspin (Sartorius Stedim Biotech) centrifugation in 0.9% NaCl. For ^{89}Zr-MSLN quality control, size-exclusion ultra-performance liquid chromatography was used with a TSK-Gel SW column G3000SWXL (5 μm, 7.8 mm; Joint Analytic Systems), elution buffer phosphate-buffered saline (140.0 mM NaCl, 9.0 mM Na_2HPO_4, 1.3 mM NaH_2PO_4), and a 0.7 mL/min flow rate (absorbance detection, 280 nm; radioactivity detection). Radiochemical purity was assessed by trichloroacetic acid precipitation assay (*26*). To determine the immunoreactive fraction, a 10-fold molar excess of recombinant MSLN extracellular domain (catalog no. 3265-MS-050; R&D Systems) was added to ^{89}Zr-MSLN and assessed by radioactivity chromatogram overlay peak intersection of bound ^{89}Zr-MSLN versus unbound ^{89}Zr-MSLN.

Cell Lines

BxPc3 human pancreatic and OVCAR3 human ovarian cancer cells were obtained from American Type Culture Collection, and HT29-MSLN transfected human colon cancer cells were obtained from Bayer AG, generated at Natural and Medical Sciences Institute (respectively, 4,200, 37,877, and 242,413 MSLN molecules per cell) (*13*). All cell lines were *Mycoplasma*-negative. The genetic origin of the cell lines was authenticated by BaseClear using short-tandem-repeat profiling. BxPc3 and OVCAR-3 cells were cultured in Dulbecco modified Eagle medium/Ham F12, and HT29-MSLN cells were cultured in RPMI 1640 medium and hygromycin B, 600 μg/mL. All cells were cultured in 10% fetal calf serum and 1% penicillin/streptomycin and were incubated at 37°C, with 5% CO_2 in a humidified incubator.

Animal Studies

Animal experiments conformed with animal welfare laws in The Netherlands and Norway. Female nude mice, 4–10 wk old and weighing 25–35 g, received 200 μg of irrelevant IgG2A (Sigma-Aldrich) within 24 h before ^{89}Zr-MSLN, ^{89}Zr-control, or ^{227}Th-MSLN injection to limit unspecific uptake in liver and spleen (*27*). A 20-μg dose was used as the standard dose, in line with published data (*13*). To investigate ^{89}Zr-MSLN dose effect, 4 and 20 μg of ^{89}Zr-MSLN were applied, equaling 0.14 mg/kg and 0.75 mg/kg in a previous publication (*13*) with an additional dose of 40 μg. Only a 20-μg nonspecific ^{89}Zr-control was used, as we were not expecting a dose effect. Tumor volumes were measured with calipers and calculated with the formula [long side × short side^2]/2, expressed as cubic millimeters. Mice with similar tumor sizes were balanced between groups. Ex vivo tissue uptake between ^{89}Zr-MSLN and ^{227}Th-MSLN was compared in female BALB/c nude-Foxn1^{nu} mice (Janvier Labs). In this experiment, inclusion of 25–30 mm^3 tumor sizes was accepted given the challenging tumor growth of the OVCAR-3 model. For PET experiments, Female NMRI-Foxn1^{nu} mice (Taconic Biosciences) were used, enabling direct comparison with published data (*13*). To reliably quantify PET data, the inclusion criterion for the imaging studies was a tumor size of more than 150 mm^3. Therefore, the OVCAR-3 tumor model was excluded for PET imaging.

To investigate ^{89}Zr-MSLN tumor and healthy tissue uptake, dose effect, and radioactive dimers, NMRI-Foxn1^{nu} mice were inoculated with 1.0 × 10^6 HT29-MSLN cells 14 d or 2.5 × 10^6 BxPc3 cells 21 d before the start of PET studies. HT29-MSLN tumor–bearing mice received 20 μg of ^{89}Zr-MSLN or ^{89}Zr-control (3–4 MBq, n = 6). BxPc3 tumor–bearing mice received 4, 20, or 40 μg of ^{89}Zr-MSLN or 20 μg of ^{89}Zr-control (1–5 MBq, n = 6). Given radioactive dimer formation, we did not exceed 40 μg. Only 20- and 40-μg dose groups could undergo PET imaging 24, 72, and 168 h after injection. Ex vivo biodistribution was performed for all groups at 168 h after injection. The effect of radioactive dimers on tissue uptake was tested at 4 μg of ^{89}Zr-MSLN with 10% versus 60% radioactive dimers in BxPc3 tumor–bearing mice. Female BALB/c nude-Foxn1^{nu} mice were inoculated with 1.0 × 10^6 HT29-MSLN cells 5 d or 5.0 × 10^6 OVCAR-3 cells 28 d before comparison of ex vivo tissue uptake of ^{89}Zr-MSLN versus ^{227}Th-MSLN. Mice received 20 μg of ^{89}Zr-MSLN (0.20 MBq) or 20 μg of ^{227}Th-MSLN (0.015 MBq) and were killed 0.5, 2, 6, 24, 72, and 168 h after injection (n = 4–5). To study whether ^{89}Zr-MSLN PET tumor uptake coincided with ^{227}Th-MSLN antitumor activity, BxPc3

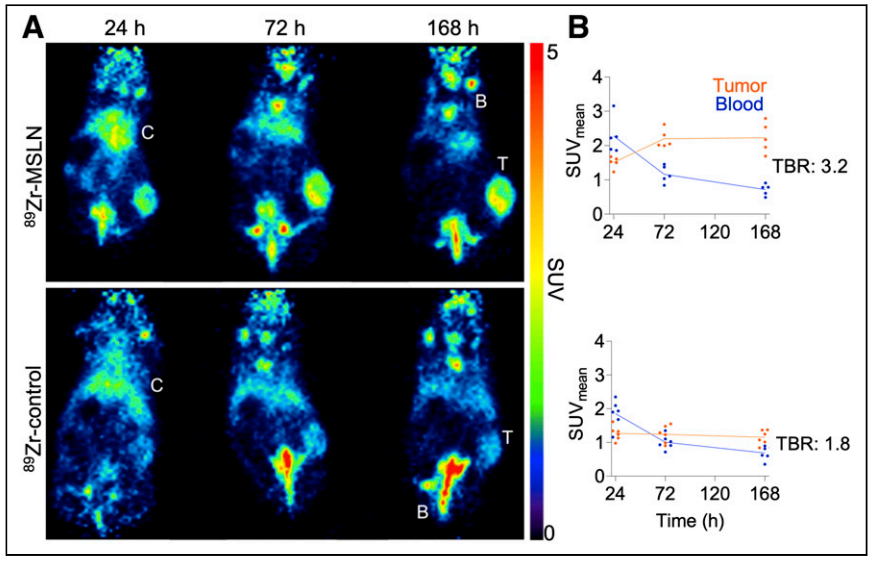

FIGURE 1. In vivo tumor uptake and biodistribution in ^{89}Zr-MSLN HT29-MSLN tumor–bearing mice (6 per group). (A) Representative coronal PET images at 24, 72, and 168 h after injection of 20 μg of ^{89}Zr-MSLN and 20 μg of ^{89}Zr-control (3–4 MBq). Uptake is presented as SUV. (B) PET quantification of ^{89}Zr-MSLN and ^{89}Zr-control uptake in tumor and blood at 24, 72, and 168 h after injection. ^{89}Zr-MSLN and ^{89}Zr-control uptake is shown as SUV_{mean} ± SD. Tumor-to-blood ratio is indicated at 168 h. B = bone; C = circulation; T = tumor; TBR = tumor-to-blood ratio.

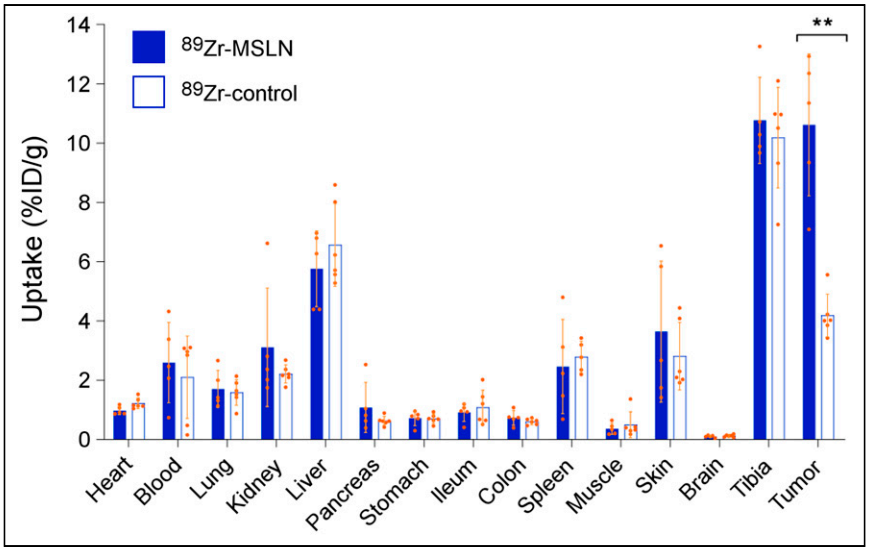

FIGURE 2. Ex vivo tumor uptake and biodistribution of ^{89}Zr-MSLN HT29-MSLN tumor–bearing mice (6 per group). Shown is ex vivo tumor and healthy tissue uptake of 20 μg of ^{89}Zr-MSLN and 20 μg of ^{89}Zr-control at 168 h after injection. Data are %ID/g, as mean ± SD; ^{89}Zr-MSLN and ^{89}Zr-control batches each contained 30% radioactive dimers. $^{*}P < 0.05$. $^{**}P < 0.01$.

and HT29-MSLN tumor–bearing NMRI-Foxn1^{nu} mice underwent ^{89}Zr-MSLN PET imaging 168 h after injection (4 MBq, 20 μg) and received a 0.75 mg/kg (500 kBq/kg) dose of ^{227}Th-MSLN 5 d after imaging (n = 7–8, no treatment: n = 2). In this time frame, no changes in MSLN tumor expression were to be expected. Tumor sizes were measured until 21 d after treatment.

The mice were imaged with a Focus 220 PET scanner (CTI Siemens). PET data were reconstructed and corrected for decay, random coincidences, scatter, and attenuation. Tumor and heart uptake was quantified with PMOD software, version 4.004, as SUV_{mean}. Ex vivo blood and tissues were weighed and radioactivity measured in a Wizard γ-counter (Perkin-Elmer) or a germanium detector (Ortec). Ex vivo uptake was expressed as percentage injected dose per gram (%ID/g).

Ex Vivo Analysis of Plasma and Tumor

Tracer integrity of ^{89}Zr-MSLN in the plasma of mice killed at 168 h after injection was studied by sodium dodecyl sulfate polyacrylamide gel electrophoresis. Mini-Protean TGX precast protein gels, 4%–15% (BioRad), were loaded with 80 μg of plasma protein. A control sample including intact tracer and free ^{89}Zr was generated by storing ^{89}Zr-MSLN at room temperature for a week. Gels ran for 30–45 min at 100 V. Formalin-fixed tumor tissues were paraffin-embedded and sliced into 4-μm sections. Gels and tumor sections were exposed overnight to a multipurpose phosphor plate (PerkinElmer) at −20°C and captured with Cyclone phosphor imager (PerkinElmer).

MSLN immunohistochemistry was executed on the autoradiography tumor sections, as described earlier (*28*). A Ventana Discovery automated stainer was used. After washing, the primary anti-MSLN antibody (clone SP74; Spring Biosciences) at 0.25 mg/mL was detected with horseradish peroxidase–labeled antimouse polymer (Dako) and 3,3′-diaminobenzidine solution. Sections were fixed at 4°C for 5 min, air-dried, and washed with double-distilled H_2O before incubation with Dako blocking solution (10 min, room temperature). After washing, primary antibody was detected with horseradish peroxidase–labeled antimouse polymer (Dako) and 3,3′-diaminobenzidine solution. Hematoxylin–eosin staining was performed on adjacent tumor sections. Digital scans were acquired by a Hamamatsu NanoZoomer 2.0-HT multislide scanner and analyzed with NanoZoomer Digital Pathology viewer software.

Statistical Analysis

Similarity between 2 groups was analyzed using a Mann–Whitney U test. When there were multiple groups or time points, a Bonferroni multiple-comparison correction was applied. All data are presented with SD. All statistical tests were performed in GraphPad Prism 8, and P values of less than 0.05 were considered significant.

RESULTS

Quality Control ^{89}Zr-MSLN

^{89}Zr-MSLN was produced with a radiolabeling efficiency of 64% ± 10%, a radiochemical purity of 98% ± 1%, and 4% ± 1%

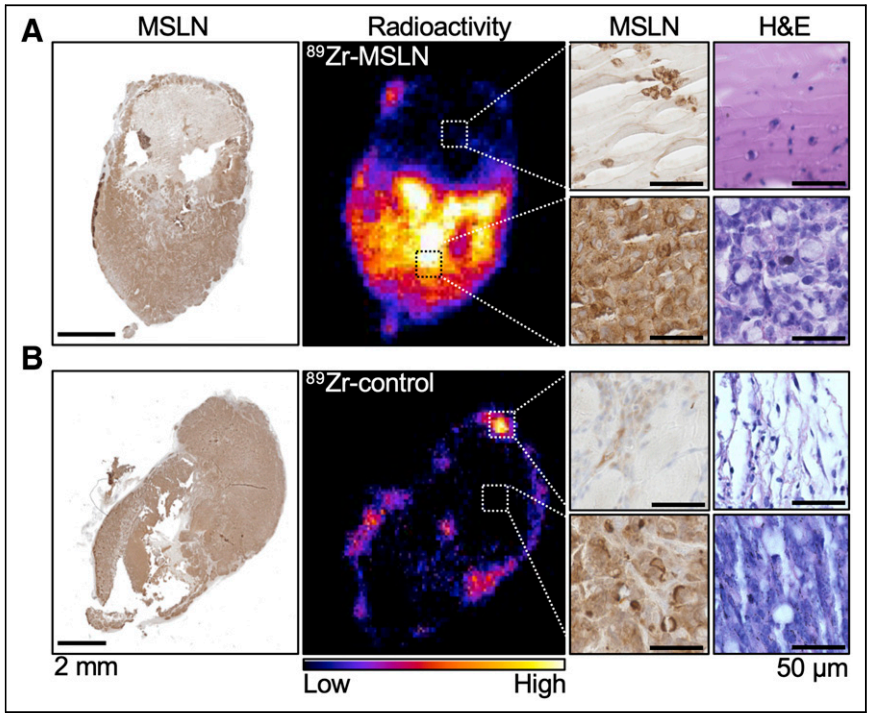

FIGURE 3. Intratumoral ^{89}Zr-MSLN distribution. Shown is MSLN immunohistochemistry, autoradiography, and hematoxylin and eosin staining of HT29-MSLN and formalin-fixed, paraffin-embedded tumor sections that received ^{89}Zr-MSLN (A) or ^{89}Zr-control (B). MSLN immunohistochemistry and autoradiography were performed on same tumor section, and hematoxylin and eosin staining were performed on adjacent tumor section. Radioactivity in A and B is simultaneously scaled, shown from high to low ^{89}Zr signal intensity. Representative data are shown (n = 3–5; rest are shown in Supplemental Fig. 2). H&E = hematoxylin and eosin.

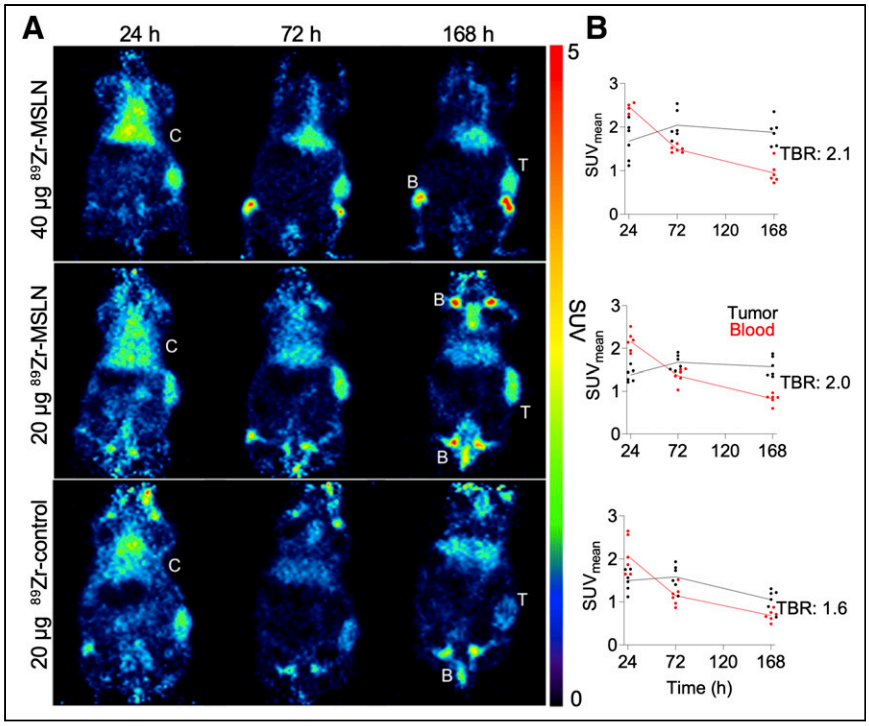

FIGURE 4. Dose effect of ^{89}Zr-MSLN on tumor uptake and biodistribution in BxPc3 tumor–bearing mice (5–6 per group). (A) Representative coronal PET images of 40 μg and 20 μg of ^{89}Zr-MSLN and 20 μg of ^{89}Zr-control at 24, 72, and 168 h after injection. Uptake is presented as SUV. (B) Quantification of tumor and blood at 24, 72, and 168 h after injection, shown as SUV_{mean} ± SD. Tumor-to-blood ratio is indicated at 168 h. B = bone; C = circulation; T = tumor; TBR = tumor-to-blood ratio.

antibody dimers and 15% ± 2% radiolabeled dimers (n = 6) (Supplemental Fig. 1A; supplemental materials are available at http://jnm.snmjournals.org). The immunoreactive fraction was 0.8 (Supplemental Fig. 1B). We observed by radioactive detection that ^{89}Zr-MSLN tended to dimerize, not observed at 280 nm. Favorable and unfavorable conditions are shown in Supplemental Table 1. The radiolabeling conditions and quality control results of the experiments are shown in Supplemental Figures 1C and 1D and Supplemental Table 2.

Tumor Uptake and Biodistribution of ^{89}Zr-MSLN

PET evaluation of ^{89}Zr-MSLN in HT29-MSLN tumor–bearing mice showed 1.8-fold higher tumor uptake and tumor-to-blood ratio for ^{89}Zr-MSLN than for ^{89}Zr-control (SUV_{mean}, 2.2 ± 0.5 vs. 1.2 ± 0.2 168 h after injection, P = 0.0043; Figs. 1A and 1B). Ex vivo biodistribution confirmed the PET data, showing 2.5-fold higher tumor uptake of ^{89}Zr-MSLN than of ^{89}Zr-control at 168 h (10.6% ± 2.4% vs. 4.2% ± 0.7 %ID/g, P = 0.0043), whereas uptake in all other tissues was similar (Fig. 2). No low-molecular-weight species of ^{89}Zr-MSLN or free ^{89}Zr were present in blood 168 h after injection (Supplemental Fig. 1E). Autoradiography showed MSLN-specific ^{89}Zr-MSLN tumor uptake compared with ^{89}Zr-control (Fig. 3; Supplemental Figs. 2A and 2B).

Dose Effect of ^{89}Zr-MSLN on Tumor Uptake and Biodistribution

In vivo, uptake and tumor-to-blood ratios were lower in ^{89}Zr-MSLN BxPc3 tumors than in HT29-MSLN tumors. ^{89}Zr-MSLN BxPc3 tumor uptake and tumor-to-blood ratios were similar between 20 μg and 40 μg (SUV_{mean}, 1.6 ± 0.2 vs. 1.9 ± 0.3) and higher than in 20-μg ^{89}Zr-control (SUV_{mean}, 1.1 ± 0.2; Figs. 4A and 4B). Ex vivo, ^{89}Zr-MSLN tumor and liver uptake were higher at 40 μg than at 4 μg 168 h after injection. In addition, mice that received 4 μg of ^{89}Zr-MSLN with 60% radioactive dimers showed higher tumor (10.0% ± 2.2% vs. 6.1% ± 1.7 %ID/g) and liver (8.8% ± 1.4% vs. 4.9% ± 1.2 %ID/g) uptake compared with mice that received 4 μg of ^{89}Zr-MSLN with 10% radioactive dimers. The excretion rate was not affected by radioactive dimers. Bone uptake was mainly in cortical bone and not in bone marrow (Supplemental Figs. 3A–3D).

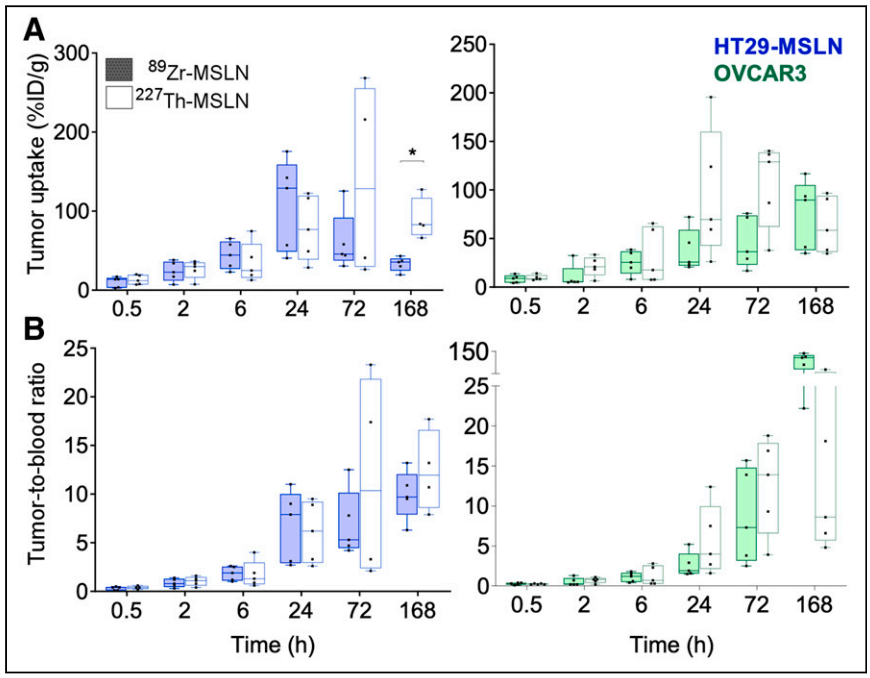

FIGURE 5. Tumor uptake of ^{89}Zr-MSLN compared with ^{227}Th-MSLN. (A and B) HT29-MSLN tumor uptake and OVCAR3 tumor uptake (A) and respective tumor-to-blood ratios (B) of 20 μg of ^{89}Zr-MSLN (0.20 MBq) vs. 20 μg of ^{227}Th-MSLN (0.015 MBq) total antibody dose at 0.5, 2, 6, 24, 72, and 168 h. Data are median %ID/g and interquartile range, including single data points. *P < 0.05 with Bonferroni adjustment.

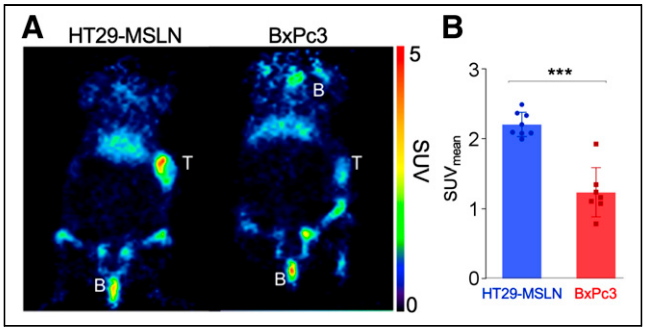

FIGURE 6. ^{89}Zr-MSLN PET before ^{227}Th-MSLN treatment. (A) Representative coronal PET images of HT29-MSLN and BxPc3 tumor–bearing mice 168 h after 20 μg of ^{89}Zr-MSLN. Tumor uptake is presented as SUV. (B) Quantification of ^{89}Zr-MSLN in HT29-MSLN and BxPc3 tumors at 168 h after injection (n = 7–8 per group). ^{89}Zr-MSLN uptake is shown as SUV_{mean} ± SD, including single data points. ***$P < 0.001$. B = bone; T = tumor.

^{89}Zr-MSLN Versus ^{227}Th-MSLN Tumor Uptake and Biodistribution

Ex vivo OVCAR3 and HT29-MSLN tumor uptake of ^{89}Zr-MSLN and ^{227}Th-MSLN was comparable except at 168 h after injection, when ^{89}Zr-MSLN HT29-MSLN tumor uptake was lower (33.1% ± 9.0% vs. 89.8% ± 26.3 %ID/g, $P = 0.016$; Fig. 5A). Tumor-to-blood ratios were similar for ^{89}Zr-MSLN and ^{227}Th-MSLN in both models (Fig. 5B). ^{89}Zr-MSLN liver uptake was higher than ^{227}Th-MSLN uptake up to 24 h in HT29-MSLN tumor–bearing mice but not at 72 and 168 h, the clinically relevant time points. ^{89}Zr-MSLN femur uptake was higher than ^{227}Th-MSLN uptake from 24 to 168 h in both models—for example, 12.3% ± 1.3 %ID/g versus 4.9% ± 0.6 %ID/g 168 h after injection in the HT29-MSLN tumor–bearing mice, resulting in lower blood and kidney levels at 72 h and 168 h (Supplemental Figs. 4A and 4B).

^{89}Zr-MSLN PET Before ^{227}Th-MSLN Treatment

^{89}Zr-MSLN PET imaging before ^{227}Th-MSLN treatment revealed 1.8-fold higher tumor SUV_{mean} in HT29-MSLN than in BxPc3 tumors (2.2 ± 0.2 vs. 1.2 ± 0.3, $P = 0.0003$; Figs. 6A and 6B). Because of the 18.7-d half-life of ^{227}Th, treatment effect is not observed in the first 9 d. From day 9 until day 21 after ^{227}Th-MSLN administration, HT29-MSLN tumors decreased 0.7 ± 0.1-fold in volume (from 432.4 ± 131.2 mm^3 to 317.4 ± 130.1 mm^3). Tumors of untreated mice grew individually 1.3-fold and 1.7-fold. In the same time frame, BxPc3 tumors did not grow after ^{227}Th-MSLN administration (1.0 ± 0.3-fold, 310.2 ± 166.5 mm^3 at day 9 and 288.3 ± 112.3 mm^3 at day 21) whereas tumors of untreated animals individually grew 1.4-fold (Figs. 7A and 7B). Absolute tumor growth is shown in Supplemental Figure 5. BxPc3 tumors of untreated- versus ^{227}Th-MSLN–treated animals were slightly larger at day 0. Therefore, tumor sizes were normalized to the size at day 0 (*29*). ^{227}Th-MSLN treatment increased DNA double-strand breaks compared with tumors of untreated mice, confirming the molecular mode of action of ^{227}Th-MSLN (Supplemental Figs. 6A and 6B).

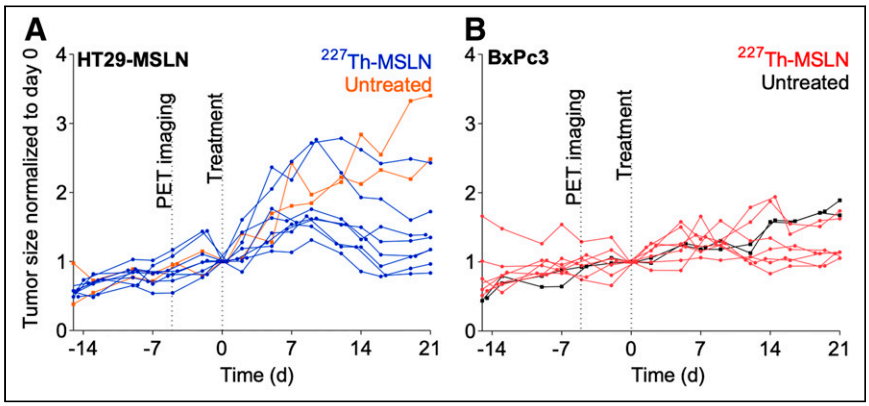

FIGURE 7. Tumor growth after ^{227}Th-MSLN treatment. (A and B) Tumor growth after ^{227}Th-MSLN treatment (0.75 mg/kg, 500 kBq/kg) in HT29-MSLN tumor–bearing mice (n = 8) (A) and in BxPc3 tumor–bearing mice (n = 7) and per model untreated mice (n = 2), normalized to day 0. Absolute tumor sizes are shown in Supplemental Figure 5.

DISCUSSION

This study showed that ^{89}Zr-MSLN PET imaging reflects ^{227}Th-MSLN tumor uptake and biodistribution in mice bearing tumors overexpressing human MSLN. We showed the dual use of an antibody–chelator conjugate, 3,2-HOPO–MSLN, radiolabeled with ^{89}Zr for PET imaging and with ^{227}Th for targeted α-therapy as a theranostic. Even though some studies have shown direct molecular imaging of ^{227}Th, this remains a challenge due to the low abundance of measurable photons in the decay chain of ^{227}Th (*30*). Studies on patients and mice showed the theranostic potential of ^{89}Zr PET for β-particle–emitting therapeutic radionuclides, such as ^{177}Lu and ^{90}Y (*31,32*). Therefore, we hypothesized that ^{89}Zr might serve as a PET surrogate radioisotope for the α-particle emitter ^{227}Th as well. Estimating ^{227}Th-MSLN whole-body distribution with ^{89}Zr-MSLN PET before treatment may be of value to guide clinical development. In addition, this study encourages ^{89}Zr-MSLN PET exploration to select patients and predict ^{227}Th-MSLN efficacy. Moreover, PET imaging with ^{89}Zr may be amenable to other targeted α-therapies.

^{89}Zr-MSLN tumor uptake might correlate with response to ^{227}Th-MSLN. However, we did not use the isogenic cell systems required to exclude differences in sensitivity to ^{227}Th-MSLN. We did not perform tumor biopsies to assess whether changes in MSLN expression occurred in the 5-d time frame between PET scan and start of treatment. A change is unlikely, as tumor growth was relatively consistent. We observed a trend in antitumor activity of ^{227}Th-MSLN comparable to the earlier in vivo study (*13*). A firm conclusion on predicting ^{227}Th-MSLN antitumor activity is precluded given the low number of animals in the control groups.

Variability in ^{89}Zr-MSLN and ^{227}Th-MSLN tumor uptake may have been a result of small tumors in the ex vivo biodistribution comparison. Higher ^{89}Zr-MSLN bone uptake might be explained by dissociated ^{89}Zr from 3,2-HOPO, tending to accumulate in the growing bone in young mice, not seen in humans (*33,34*). Ex vivo blood samples at 168 h showed intact ^{89}Zr-MSLN, indicating that the tracer available in the circulation for tissue uptake is intact. This finding suggests that free ^{89}Zr clears from the blood immediately into cortical bone. Although desferrioxamine-based chelators are commonly used for complexation with ^{89}Zr, HOPO-based chelators are a proven alternative (*35,36*). To avoid chelator-driven discrepancies in pharmacokinetics between ^{89}Zr-MSLN and ^{227}Th-MSLN (*37,38*), we developed the PET tracer using the same 3,2-HOPO–MSLN conjugate with the additional advantage of having the intermediate product clinical grade right at

hand. We showed in mice that ^{89}Zr-MSLN uptake can predict tumor targeting of ^{227}Th-MSLN. In patients, ^{89}Zr-MSLN PET imaging might detect MSLN-positive lesions in mesothelioma, ovarian cancer, and pancreatic cancer and clarify whether the antibody can reach these lesions. Yet, calculating an exact ^{227}Th radiation dose per organ is limited by the observed ^{89}Zr-MSLN bone uptake. For potential dosimetry purposes, we should aim to improve the in vivo stability of HOPO-based ^{89}Zr chelators.

Higher liver uptake of ^{89}Zr-MSLN with a high radioactive dimer content indicates faster clearance of dimers and aggregates than of monomers (*39*). Higher tumor uptake could be explained by increased retention at the target-binding site due to an avidity effect (*40*) combined with an enhanced permeability and retention effect (*41*). Higher tumor uptake at 40 μg than at 4 μg of total antibody dose may, therefore, most likely be a dimer effect instead of a dose effect. Dimerization appears specific for ^{89}Zr-3,2-HOPO because the control antibody revealed similar radioactive dimer content, not observed in combination with ^{227}Th to the same extent (*13*). In a clinical setting, the specification should be set at less than 15%. This is feasible with the optimized radiolabeling procedure that we describe.

CONCLUSION

Our study revealed the potential of ^{89}Zr-MSLN PET to predict ^{227}Th-MSLN tumor uptake and biodistribution. Furthermore, it addressed the potential of ^{89}Zr-MSLN PET as a tool to estimate ^{227}Th-MSLN antitumor activity. Our data support clinical investigation of ^{89}Zr-MSLN PET imaging in combination with ^{227}Th-MSLN therapy.

DISCLOSURE

This study was supported by a research grant from Bayer to Elisabeth de Vries. Payments were made available to her institution (University Medical Center Groningen). Bayer developed and owns the intellectual property rights of 3,2-HOPO–MSLN and ^{227}Th-MSLN. Elisabeth de Vries reports institutional financial support for a consulting and advisory role from Sanofi, Daiichi Sankyo, NSABP, Crescendo Biologics, and Cyprus Cancer Research Institute and institutional financial support for clinical trials or contracted research from Amgen, Genentech, Roche, AstraZeneca, Synthon, Regeneron, Chugai Pharma, CytomX Therapeutics, Servier, Nordic Nanovector, G1 Therapeutics, and Radius Health, all outside the submitted work. No other potential conflict of interest relevant to this article was reported.

ACKNOWLEDGMENTS

We thank Manuela Brand for performing the immunohistochemistry and immunofluorescent staining (Bayer AG) and Linda Pot-de Jong for assisting with the animal experiments (Department of Medical Oncology, University Medical Center Groningen).

KEY POINTS

QUESTION: Can ^{89}Zr-MSLN PET imaging predict ^{227}Th-MSLN behavior?

PERTINENT FINDINGS: ^{89}Zr-MSLN PET imaging shows tumor uptake and biodistribution similar to that of ^{227}Th-MSLN in MSLN-expressing tumor–bearing nude mice.

IMPLICATIONS FOR PATIENT CARE: These data support the theranostic potential of ^{89}Zr-MSLN PET imaging to guide ^{227}Th-MSLN therapy in patients.

REFERENCES

1. Christoph DC, Eberhardt WE. Systemic treatment of malignant pleural mesothelioma: new agents in clinical trials raise hope of relevant improvements. *Curr Opin Oncol.* 2014;26:171–181.
2. Herzog TJ, Monk BJ. Bringing new medicines to women with epithelial ovarian cancer: what is the unmet medical need? *Gynecol Oncol Res Pract.* 2017;4:13.
3. Parker C, Lewington V, Shore N, et al. Targeted alpha therapy, an emerging class of cancer agents: a review. *JAMA Oncol.* 2018;4:1765–1772.
4. Guerra Liberal FDC, O'Sullivan JM, McMahon SJ, Prise KM. Targeted alpha therapy: current clinical applications. *Cancer Biother Radiopharm.* 2020;35:404–417.
5. Parker C, Nilsson S, Heinrich D, et al. Alpha emitter radium-223 and survival in metastatic prostate cancer. *N Engl J Med.* 2013;369:213–223.
6. Kratochwil C, Haberkorn U, Giesel FL. Radionuclide therapy of metastatic prostate cancer. *Semin Nucl Med.* 2019;49:313–325.
7. Ramdahl T, Bonge-Hansen HT, Ryan OB, et al. An efficient chelator for complexation of thorium-227. *Bioorg Med Chem Lett.* 2016;26:4318–4321.
8. Deblonde GJ, Lohrey T, Booth C, et al. Solution thermodynamics and kinetics of metal complexation with a hydroxypyridinone chelator designed for thorium-227 targeted alpha therapy. *Inorg Chem.* 2018;57:14337–14346.
9. Hagemann UB, Wickstroem K, Hammer S, et al. Advances in precision oncology: Targeted thorium-227 conjugates as a new modality in targeted alpha therapy. *Cancer Biother Radiopharm.* 2020;35:497–510.
10. Dahle J, Borrebaek J, Jonasdottir TJ, et al. Targeted cancer therapy with a novel low-dose rate alpha-emitting radioimmunoconjugate. *Blood.* 2007;110:2049–2056.
11. Hagemann UB, Wickstroem K, Wang E, et al. In vitro and in vivo efficacy of a novel CD33-targeted thorium-227 conjugate for the treatment of acute myeloid leukemia. *Mol Cancer Ther.* 2016;15:2422–2431.
12. Hagemann UB, Mihaylova D, Uran SR, et al. Targeted alpha therapy using a novel CD70 targeted thorium-227 conjugate in in vitro and in vivo models of renal cell carcinoma. *Oncotarget.* 2017;8:56311–56326.
13. Hagemann UB, Ellingsen C, Schuhmacher J, et al. Mesothelin-targeted thorium-227 conjugate (MSLN-TTC): preclinical evaluation of a new targeted alpha therapy for mesothelin-positive cancers. *Clin Cancer Res.* 2019;25:4723–4734.
14. Hammer S, Hagemann UB, Kolbe-Zitzmann S, et al. Preclinical efficacy of a PSMA-targeted thorium-227 conjugate (PSMA-TTC), a targeted alpha therapy for prostate cancer. *Clin Cancer Res.* 2020;28:1985–1996.
15. Bera TK, Pastan I. Mesothelin is not required for normal mouse development or reproduction. *Mol Cell Biol.* 2000;20:2902–2906.
16. Chen SH, Hung WC, Wang P, Paul C, Konstantopoulos K. Mesothelin binding to CA125/MUC16 promotes pancreatic cancer cell motility and invasion via MMP-7 activation. *Sci Rep.* 2013;3:1870.
17. Rump A, Morikawa Y, Tanaka M, et al. Binding of ovarian cancer antigen CA125/MUC16 to mesothelin mediates cell adhesion. *J Biol Chem.* 2004;279:9190–9198.
18. Hassan R, Thomas A, Alewine C, Le TL, Jaffee EM, Pastan I. Mesothelin immunotherapy for cancer: ready for prime time? *J Clin Oncol.* 2016;34:4171–4179.
19. Morello A, Sadelain M, Adusumilli PS. Mesothelin-targeted CARs: driving T cells to solid tumors. *Cancer Discov.* 2016;6:133–146.
20. Zhao XY, Subramanyam B, Sarapa N, Golfier S, Dinter H. Novel antibody therapeutics targeting mesothelin in solid tumors. *Clin Cancer Drugs.* 2016;3:76–86.
21. Quanz M, Hagemann U, Zitzmann-Kolbe S, et al. Anetumab ravtansine inhibits tumor growth and shows additive effect in combination with targeted agents and chemotherapy in mesothelin-expressing human ovarian cancer models. *Oncotarget.* 2018;9:34103–34121.
22. Hassan R, Blumenschein GR Jr, Moore KN, Santin AD, Kindler HL. First-in-human, multicenter, phase I dose-escalation and expansion study of anti-mesothelin antibody-drug conjugate anetumab ravtansine in advanced or metastatic solid tumors. *J Clin Oncol.* 2020;38:1824–1835.
23. Gebhart G, Lamberts LE, Wimana Z, et al. Molecular imaging as a tool to investigate heterogeneity of advanced HER2-positive breast cancer and to predict patient outcome under trastuzumab emtansine (T-DM1): the ZEPHIR trial. *Ann Oncol.* 2016;27:619–624.
24. Lamberts LE, Menke-van der Houven van Oordt CW, ter Weele EJ, et al. Immuno-PET with anti-mesothelin antibody in patients with pancreatic and ovarian cancer before anti-mesothelin antibody–drug conjugate treatment. *Clin Cancer Res.* 2016;22:1642–1652.
25. Bensch F, van der Veen EL, Lub-de Hooge MN, et al. ^{89}Zr-atezolizumab imaging as a non-invasive approach to assess clinical response to PD-L1 blockade in cancer. *Nat Med.* 2018;24:1852–1858.
26. Nagengast WB, de Vries EG, Hospers GA, et al. In vivo VEGF imaging with radiolabeled bevacizumab in a human ovarian tumor xenograft. *J Nucl Med.* 2007;48:1313–1319.

27. Reddy N, Ong GL, Behr TM, Sharkey RM, Goldenberg DM, Mattes MJ. Rapid blood clearance of mouse IgG2a and human IgG1 in many nude and nu/þ mouse strains is due to low IgG2a serum concentrations. *Cancer Immunol Immunother.* 1998;46:25–33.
28. Golfier S, Kopitz C, Kahnert A, et al. Anetumab ravtansine: a novel mesothelin-targeting antibody–drug conjugate cures tumors with heterogeneous target expression favored by bystander effect. *Mol Cancer Ther.* 2014;13:1537–1548.
29. Hather G, Liu R, Bandi S, et al. Growth rate analysis and efficient experimental design for tumor xenograft studies. *Cancer Inform.* 2014;13:65–72.
30. Murray I, Rojas B, Gear J, Callister R, Cleton A, Flux GD. Quantitative dual-isotope planar imaging of thorium-227 and radium-223 using defined energy windows. *Cancer Biother Radiopharm.* 2020;35:530–539.
31. Perk LR, Visser GWM, Vosjan MJWD, et al. ^{89}Zr as a PET surrogate radioisotope for scouting biodistribution of the therapeutic radiometals ^{90}Y and ^{177}Lu in tumor-bearing nude mice after coupling to the internalizing antibody cetuximab. *J Nucl Med.* 2005;46:1898–1906.
32. Rizvi SNF, Visser OJ, Vosjan MJWD, et al. Biodistribution, radiation dosimetry and scouting of ^{90}Y-ibritumomab tiuxetan therapy in patients with relapsed B-cell non-Hodgkin's lymphoma using ^{89}Zr-ibritumomab tiuxetan and PET. *Eur J Nucl Med Mol Imaging.* 2012;39:512–520.
33. Deri MA, Zeglis BM, Francesconi LC, Lewis JS. PET imaging with ^{89}Zr: from radiochemistry to the clinic. *Nucl Med Biol.* 2013;40:3–14.
34. Bensch F, Smeenk MM, van Es SC, et al. Comparative biodistribution analysis across four different ^{89}Zr-monoclonal antibody tracers: the first step towards an imaging warehouse. *Theranostics.* 2018;8:4295–4304.
35. N Tinianow J, Pandya DN, Pailloux SL, et al. Evaluation of a 3-hydroxypyridin-2-one (2,3-HOPO) based macrocyclic chelator for $^{89}Zr^{4+}$ and its use for immunoPET imaging of HER2 positive model of ovarian carcinoma in mice. *Theranostics.* 2016;6:511–521.
36. Deri MA, Ponnala S, Kozlowski P, et al. HOPO p-SCN-Bn-HOPO: a superior bifunctional chelator for ^{89}Zr immunoPET. *Bioconjug Chem.* 2015;26:2579–2591.
37. Bhatt NB, Pandya DN, Wadas TJ. Recent advances in zirconium-89 chelator development. *Molecules.* 2018;23:638.
38. Heskamp S, Raavé R, Boerman O, Rijpkema M, Goncalves V, Denat F. ^{89}Zr-immuno-positron emission tomography in oncology: state-of-the-art ^{89}Zr radiochemistry. *Bioconjug Chem.* 2017;28:2211–2223.
39. Hötzel I, Theil FP, Bernstein LJ, et al. A strategy for risk mitigation of antibodies with fast clearance. *MAbs.* 2012;4:753–760.
40. Kortt AA, Dolezal O, Power BE, Hudson PJ. Dimeric and trimeric antibodies: high avidity scFvs for cancer targeting. *Biomol Eng.* 2001;18:95–108.
41. Kalyane D, Raval N, Maheshwari R, Tambe V, Kalia K, Tekade R. Employment of enhanced permeability and retention effect (EPR): nanoparticle-based precision tools for targeting of therapeutic and diagnostic agent in cancer. *Mater Sci Eng C Mater Biol Appl.* 2019;98:1252–1276.